The Astrophysical Journal, 987:63 (8pp), 2025 July 1 https://doi.org/10.3847/1538-4357/add92e

NuSTAR and XMM-Newton Observations of PSR J1930+1852 and Its Pulsar Wind Nebula

J. A. J. Alford[1,2], G.-B. Zhang[1,2,3], and J. D. Gelfand[1,2]
[1] Division of Science, NYU Abu Dhabi, PO Box 129188, Abu Dhabi, UAE; alford@nyu.edu
[2] Center for Astrophysics and Space Science (CASS), New York University Abu Dhabi, PO Box 129188, Abu Dhabi, UAE
[3] Yunnan Observatory, Kunming, Yunnan, People's Republic of China
Received 2024 September 18; revised 2025 April 15; accepted 2025 May 13; published 2025 June 27

Abstract

Synchrotron X-ray emission from a pulsar wind nebula (PWN) is a sensitive probe of its magnetic field and high-energy particle population. Here we analyze contemporaneous NuSTAR and XMM-Newton observations of the PWN G54.1+0.3, powered by pulsar PSR J1930+1852. We also present a preliminary timing analysis of the central pulsar PSR J1930+1852 and analyze its X-ray pulse profiles in different energy bands. We detect X-ray emission from the combined pulsar and PWN system up to ≈70 keV, while emission from the PWN itself has been detected up to ≈30 keV, with a photon index Γ increasing from ∼1.9 to ∼2.4 with photon energy between 3 and 30 keV. PWN G54.1+0.3's X-ray spectrum is consistent with a broken power law, with break energy $E_{\rm break} \approx 5$ keV, consistent with synchrotron cooling of a single power-law particle spectrum. The best-fit broadband spectral energy distribution model after the inclusion of this new spectral data indicates a maximum particle energy $E_{\rm max} \sim 400$ TeV. We discuss PSR J1930+1852 and PWN G54.1+0.3 in the context of other PWNe powered by young energetic pulsars.

Unified Astronomy Thesaurus concepts: Pulsar wind nebulae (2215); Supernova remnants (1667); Pulsars (1306)

1. Introduction

Young rotation-powered pulsars are known sources of intense nonthermal X-ray emission. These nonthermal X-rays can be produced by relativistic particles in both the neutron star magnetosphere and surrounding pulsar wind nebula (PWN). In the case of PWN emission, the $e^{\pm}$ streaming through the PWN emits both synchrotron and inverse Compton (IC) radiation, which can be observed across the electromagnetic spectrum, from radio to γ-rays (see P. Slane 2017 for a review of PWNe). At X-ray energies, the dominant contribution is synchrotron emission, whose properties depend on both the magnetic field strength and the particle spectrum within the PWN. In contrast, the PWN's IC emission, which dominates the spectral energy distribution (SED) at γ-ray energies, is determined by the particle and target photon spectra and is independent of the magnetic field. Therefore, modeling the broadband PWN SED probes both the B field and particle spectrum within the PWN.

PWN G54.1+0.3 is similar in many respects to the Crab Nebula, with Chandra observations revealing that both are young PWNe characterized by a central pulsar point source, a ring, jets, and a surrounding diffuse synchrotron nebula (F. J. Lu et al. 2002; F. Bocchino et al. 2010; T. Temim et al. 2010). G54.1+0.3 is among the several PWNe (e.g., 3C 58 and the Crab Nebula) that lack an obvious shell associated with a supernova remnant (SNR) forward shock. It is not clear if the SNR ejecta have not yet been shocked or more sensitive X-ray and radio observations will reveal the SNR shell. Radio and X-ray shells associated with G54.1+0.3's forward shock have been suggested but not confirmed (F. Bocchino et al. 2010; S. Goedhart et al. 2024; K. Tsalapatas et al. 2024).

G54.1+0.3 is powered by the 137 ms pulsar PSR J1930+1852, with a large spin-down power $\dot{E} \equiv 4\pi^2 I \frac{P}{\dot{P}^3} = 1.2 \times 10^{37}$ erg s^{-1} and young characteristic age $\tau_{\rm ch} \equiv P/2\dot{P} \approx 2900$ yr (F. Camilo et al. 2002). The pulsar X-ray spectrum is nonthermal and is consistent with a single power law with a photon index $\Gamma = 1.44 \pm 0.04$ (T. Temim et al. 2010). Similarly, the PWN's X-ray spectrum is also nonthermal, with a photon index $\Gamma \sim 1.8$ and an unabsorbed flux ∼5× greater than the pulsar the 0.2 −10 keV band.

Recently, the Large High Altitude Air Shower Observatory (LHAASO) reported the detection of $\gtrsim$100 TeV γ-rays from 43 sources (Z. Cao et al. 2024). G54.1+0.3 is located $\leqslant 0.^{\circ}29$ from one of these γ-ray sources: 1LHAASO J1929+1846u. G54.1+0.3 may therefore be a PeVatron like the Crab Nebula, although there are other potential γ-ray sources nearby.

Measurements of G54.1+0.3's X-ray synchrotron emission are required to investigate G54.1+0.3's potential to accelerate particles to energies $\gtrsim$100 TeV. We have obtained coordinated NuSTAR and XMM-Newton observations of G54.1+0.3, in order to measure its broadband (0.5–80 keV) X-ray spectrum. These X-ray spectral measurements are also essential inputs in broadband SED modeling of G54.1+0.3, which will also help determine if G54.1+0.3 is producing the $\gtrsim$100 TeV γ-rays observed by LHAASO.

In this paper, we present a comprehensive analysis of the broadband X-ray spectrum of the pulsar PSR J1930+1852 and its PWN G54.1+0.3 with these XMM-Newton and NuSTAR observations. This paper is structured as follows: In Section 2, we describe the observations, data reduction, and analysis methods. In Section 3, we present the results of the temporal and spectral analysis of these data. In Section 4, we present an SED model of the PWN in G54.1+0.3, updated with these new X-ray spectral data points. We discuss the implications of these results in Section 5 and summarize our findings in Section 6.

Table 1
Log of X-Ray Observations

Date (UT)	Observatory	ObID	Instr./Mode	Exposure (ks)
2016 Mar 27	XMM-Newton	0762980101	EPIC-MOS1/ Full Frame	108.7
…	…	…	EPIC-MOS2/ Full Frame	108.6
…	…	…	EPIC-pn/Full Frame	108.9
2016 Mar 27	NuSTAR	40101006002	FPMA	54.3
…	…	…	FPMB	54.1
2016 Jul 2	NuSTAR	40201012002	FPMA	80.1
…	…	…	FPMB	80.0

2. Data Reduction

2.1. NuSTAR

NuSTAR (F. A. Harrison et al. 2013) observed G54.1+0.3 on 2016 March 27 and again on 2016 July 2 (Table 1). The standard data reduction pipeline NUPIPLINE was run with CALDB version 20240701. Spectra were extracted from the two NuSTAR focal plane modules, FPMA and FPMB, using circular regions with a 1.′25 radius centered at the source position and circular background regions with a 2.′25 radius (see Figure 1). The spectra were binned to ensure a minimum of 25 counts per bin.

2.2. XMM-Newton

XMM-Newton observed G54.1+0.3 for 108 ks on 2016 March 27 (ObsID 0762980101). The XMM-Newton data were analyzed using the standard XMM scientific analysis software (SAS) version XMMSAS_20160201_1833–15.0.0 with the latest calibration files. We created reprocessed event files for EPIC-PN, EPIC-MOS1, and EPIC-MOS2 using the tasks EPPROC and EMPROC.

Time intervals affected by solar flares were removed, reducing the useful exposure time to ∼52 ks. We then extracted source spectra from PN, MOS1, and MOS2 using circular regions with a 1′ radius radius centered at the source position. We selected circular source-free background regions with a 1.′5 radii on the same CCD (Figure 1). We created redistribution matrices and ancillary files using the SAS tools RMFGEN and ARFGEN, respectively. The spectra were binned to ensure a minimum of 25 counts per bin.

2.2.1. Search for Diffuse X-Ray Emission

Previous studies reported diffuse X-ray emission extending out to ≈400″ from PSR J1930+1852, potentially associated with G54.1+0.3's SNR shell (F. Bocchino et al. 2010). Figure 2 shows zoomed-in, exposure, and vignetting-corrected images from the XMM-Newton MOS1, MOS2, and PN detectors. The radial surface brightness profiles in the right panel of Figure 2 indicate the diffuse emission extends out no more than 100″ from PSR J1930+1852. This X-ray extension of the G54.1+0.3 PWN is consistent with the ∼80″ radius of the infrared dust shell (T. Temim et al. 2017).

3. Data Analysis

3.1. Timing Analysis

We searched for PSR J1930+1852's pulsed X-ray emission by extracting photons from within a 1′ radius around the pulsar and calculating the photon arrival times at the solar system barycenter. The photon arrival times from the FPMA and FPMB detectors were combined to calculate the power density spectra shown in Figure 3 (D. A. Leahy et al. 1983). We identified a clear periodic signal at ≈137 ms (Figure 3), consistent with previous detections (F. Camilo et al. 2002; F. Lu et al. 2007). The central peaks at each epoch correspond to pulsar rotation periods $P = 137.192387(3)$ ms and $P = 137.198727(2)$ ms. Table 2 lists these two NuSTAR measurements of PSR J1930+1852's rotation period, along with previous measurements.

F. Camilo et al. (2002) used radio observations separated by 8 months to measure $\dot{P} = 7.5057(1) \times 10^{-13}\,\mathrm{s\,s^{-1}}$. Extrapolating from their precisely measured 2002 January 17 spin period to the NuSTAR-measured periods in Table 2, we calculate a larger long-term $\dot{P} = 7.517(3) \times 10^{-13}\,\mathrm{s\,s^{-1}}$, consistent with the $\dot{P} = 7.514(4) \times 10^{-13}\,\mathrm{s\,s^{-1}}$ inferred from the change in spin period between the two NuSTAR observations. This increase in the long-term $\dot{P}$ implies that PSR J1930+1852's braking index $n < 2$. A detailed timing analysis will be discussed by J. A. J. Alford et al. 2025 (in preparation).

In order to check for phase-dependent spectral variations, we calculated the hardness ratio (HR) in each phase bin. We define $\mathrm{HR} = N_h/N_s$, where N_s and N_h are the count rates in the 3–10 and 10–30 keV energy bands, respectively. Normalized HRs are shown in the lower-right panels of Figure 3. We find that PSR J1930+1852's on-pulse emission is harder than the off-pulse emission.

3.2. Spectral Analysis

X-ray spectral analysis was performed using `HEASoft` version 16.33 and of the `Xspec` version 12.14.0 (K. A. Arnaud 1996). Throughout this spectral modeling, we have used the Tuebingen–Boulder X-ray absorption model `tbabs` with elemental abundances from J. Wilms et al. (2000).

The NuSTAR spectrum of the G54.1 PWN includes X-rays from the pulsar PSR J1930+1852 because NuSTAR cannot spatially resolve the pulsar from the PWN. Since we want to include only PWN emission in our SED modeling, we include a power-law spectral component in our analysis to account for the spectrum of PSR J1930+1852. We explored a phase-resolved spectroscopic analysis, treating the off-pulse spectrum as pure background PWN emission, and found that the derived pulsar spectrum differed from the uncontaminated Chandra spectrum reported by T. Temim et al. (2010). This could be due to significant unpulsed nonthermal X-ray emission from the pulsar contaminating the "off" spectrum. Considering the large NuSTAR point-spread function (PSF), we chose to adopt the results of the Chandra analysis for the pulsar spectrum. The power-law index Γ and normalization of the pulsar component were fixed to the values obtained from a previous Chandra observation with $\Gamma_{\mathrm{psr}} = 1.44 \pm 0.04$ (T. Temim et al. 2010). We have confirmed that T. Temim et al. (2010) used the same Wilms abundances in their absorption model (T. Temim 2025, private communication).

Holding the pulsar's spectral parameters fixed, we then fit models for the pulsar and PWN emission to the joint XMM-

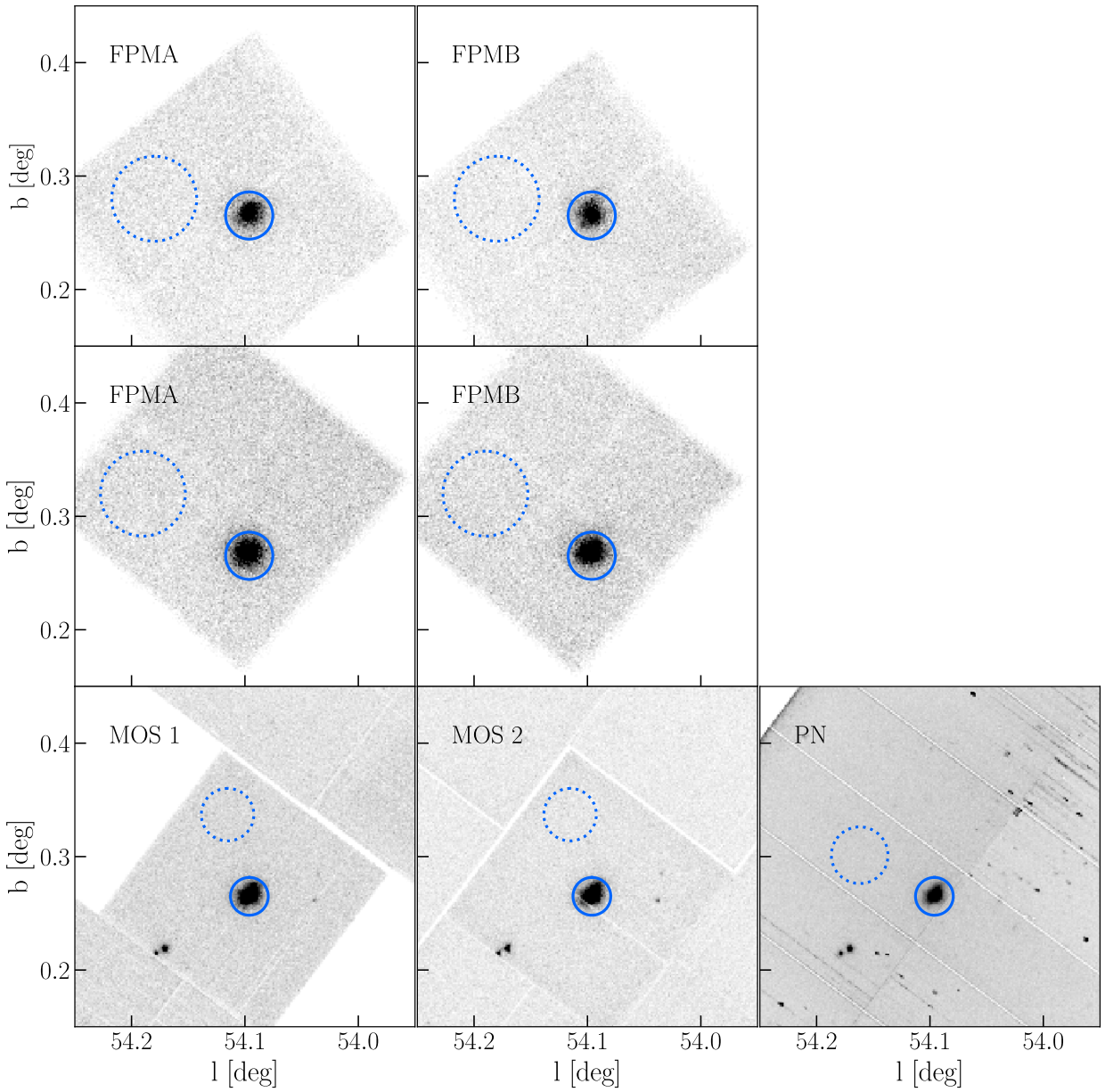

Figure 1. X-ray images of G54.1+0.3. Solid (dotted) circles indicate the source (background) spectral extraction regions for the NuSTAR and XMM-Newton observations.

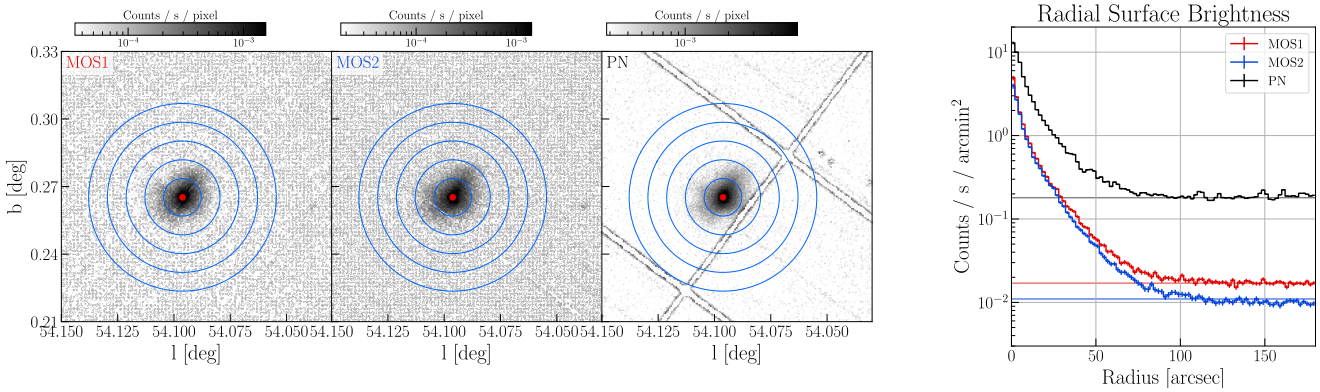

Figure 2. Left: exposure and vignetting-corrected XMM-Newton images of G54.1+0.3, scaled to highlight weak diffuse X-rays from the PWN. The brightest emission coincides with the position of the pulsar (red point), and blue rings indicate radial distance in units of 30″. Right: radial surface brightness measured by the XMM-Newton MOS1, MOS2, and PN detectors. Horizontal lines indicate the background surface brightness of each detector.

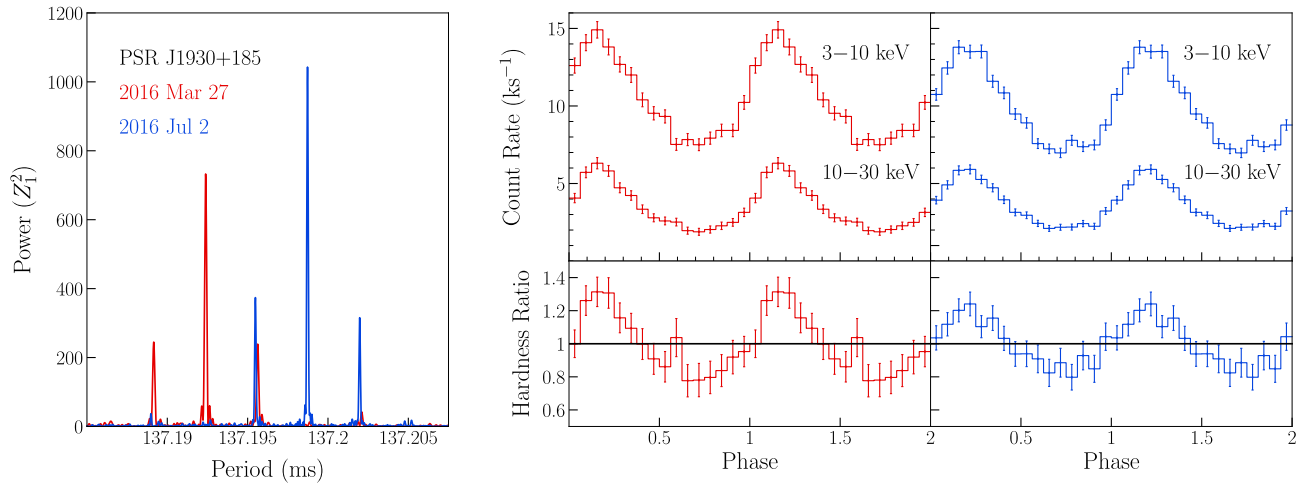

Figure 3. Left: Z_1^2 power density spectra in each of the two NuSTAR observations, with the central peaks at each epoch corresponding to periods $P = 137.192387$ (3) ms and $P = 137.198727(2)$ ms. Upper right: background-subtracted pulse profiles in the 3−10 and 10−30 keV bands. Lower right: normalized HR (10−30 keV count rate/3−10 keV count rate) as a function of the rotational phase.

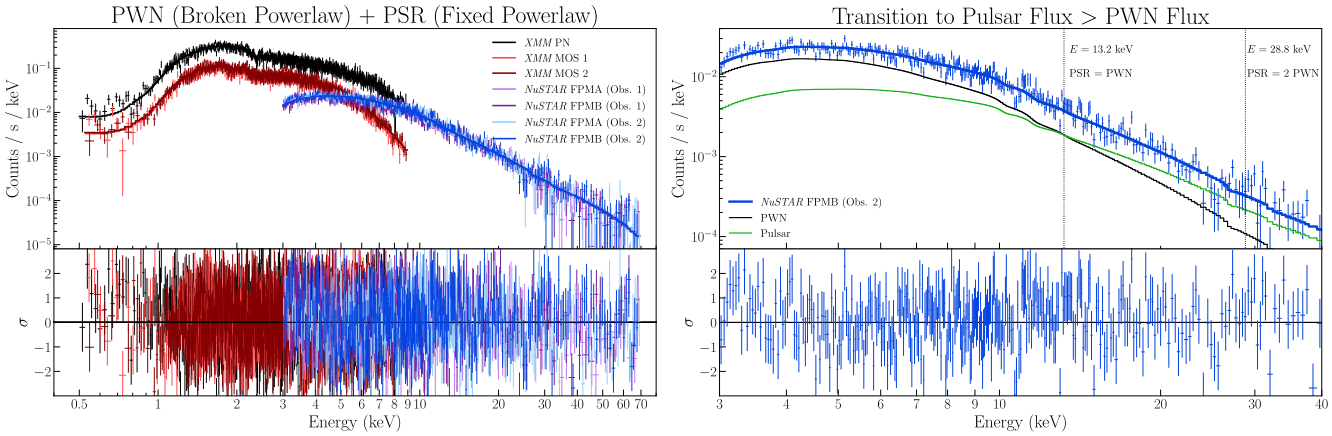

Figure 4. Left: joint XMM-Newton and NuSTAR spectra fit with a broken power-law plus pulsar power-law (BKN+POW) model. The parameters of the pulsar power-law model were fixed to the values determined from a previous Chandra observation. Right: the G54.1+0.3 spectrum from the second, longer NuSTAR observation, focusing on the energy range where the pulsar flux becomes dominant over the PWN flux.

Table 2
Measurements of PSR J1930+1852's Rotation Period

Date (UT)	Observatory	Period (ms)	References
1997 Apr 27	ASCA	136.74374(5)	(1)
2002 Jan 17	Arecibo	136.855046957(9)	(1)
2002 Sep 12	RXTE	136.871312(4)	(2)
2002 Dec 23	RXTE	136.877919(3)	(2)
2003 Jun 30	Chandra	136.890130(5)	(2)
2016 Mar 27	NuSTAR	137.192387(3)	This work
2016 Jul 2	NuSTAR	137.198727(2)	This work

References. (1) F. Camilo et al. (2002); (2) F. Lu et al. (2007).

Newton–NuSTAR spectra. We include data from the two XMM MOS detectors, the XMM PN detector, and the two NuSTAR detectors. We explored a power-law model and a broken power-law model (CONST*TBABS(POW+BKNPOW), hereafter PL+BKN) or two single power-law models (CONST*TBABS(POW+POW), hereafter PL+PL) in the 0.5–70 keV energy band. The constant factors CONST were multiplied by the spectra from each detector in order to account for systematic calibration offsets. The factors differed by <1% between the NuSTAR A and B modules and <10% between XMM-Newton and NuSTAR.

The joint XMM-Newton-NuSTAR spectrum (Figure 4) shows curvature, especially above ∼5 keV, which is more consistent with the PL+BKN model than the PL+PL model, and this is reflected in the χ^2 values listed in Table 3. We checked that the spectral curvature is intrinsic to the G54.1+0.3 spectrum, and not an artifact of the relative XMM-Newton–NuSTAR calibration, by confirming that the XMM-Newton data alone are more consistent with the PL+BKN model versus the PL+PL model. We explored keeping the absorption column fixed at the value $N_{\rm H} = (1.95 \pm 0.03) \times 10^{22}\,{\rm cm}^{-2}$ found by T. Temim et al. (2010) and also allowing $N_{\rm H}$ to vary. A slightly lower $N_{\rm H} \approx 1.5 \times 10^{22}\,{\rm cm}^{-2}$ value is preferred by the joint XMM-Newton–NuSTAR spectra. Table 3 lists the spectral modeling results for both the PL+BKN and PL+PL models for both $N_{\rm H}$ values. The left panel of Figure 4 shows the joint fit of the NuSTAR and XMM-Newton data to the PL+BKN model. The right panel of Figure 4 shows the individual contributions of

Table 3
Joint Fits to XMM-Newton and NuSTAR Spectra

Model	N_H (10^{22} cm^{-2})	Γ_{psr}	Pulsar Flux[a] (10^{-12} erg cm^{-2} s^{-1})	Γ_1	E_break (keV)	Γ_2	PWN Flux[a] (10^{-12} erg cm^{-2} s^{-1}))	χ^2 (dof)
PL+PL	$1.73^{+0.02}_{-0.03}$	1.4 (fixed)	5.1 (fixed)	$2.10^{+0.03}_{-0.03}$	⋯	⋯	$6.6^{+0.1}_{-0.1}$	3881 (3736)
PL+PL	$1.71^{+0.02}_{-0.03}$	1.44 (fixed)	5.1 (fixed)	$2.06^{+0.02}_{-0.02}$	⋯	⋯	$6.4^{+0.1}_{-0.1}$	3822 (3736)
PL+PL	$1.69^{+0.02}_{-0.02}$	1.48 (fixed)	5.1 (fixed)	$2.02^{+0.02}_{-0.02}$	⋯	⋯	$6.4^{+0.1}_{-0.1}$	3781 (3736)
PL+BKN	$1.51^{+0.03}_{-0.04}$	1.4 (fixed)	5.1 (fixed)	$1.83^{+0.04}_{-0.06}$	$5.5^{+0.4}_{-0.5}$	$2.46^{+0.07}_{-0.08}$	$5.8^{+0.1}_{-0.1}$	3618 (3734)
PL+BKN	$1.50^{+0.04}_{-0.03}$	1.44 (fixed)	5.1 (fixed)	$1.78^{+0.08}_{-0.08}$	$5.1^{+0.6}_{-0.3}$	$2.32^{+0.07}_{-0.05}$	$5.8^{+0.2}_{-0.1}$	3572 (3734)
PL+BKN	$1.49^{+0.03}_{-0.03}$	1.48 (fixed)	5.1 (fixed)	$1.75^{+0.04}_{-0.05}$	$5.0^{+0.4}_{-0.4}$	$2.24^{+0.05}_{-0.05}$	$5.8^{+0.1}_{-0.1}$	3564 (3734)

Notes. The pulsar contribution to the combined pulsar-plus-PWN spectrum is modeled with a single power law, with its flux and photon index Γ_{psr} held fixed at the Chandra-derived values (T. Temim et al. 2010).
[a] Unabsorbed flux in the 3−30 keV band.

Table 4
G54.1+0.3 PWN Spectrum in the 3−30 keV Band

Energy Band (keV)	N_H (10^{22} cm^{-2})	Γ_{psr}	Pulsar Flux[a] (10^{-12} erg cm^{-2} s^{-1})	Γ_{pwn}	PWN Flux[a] (10^{-12} erg cm^{-2} s^{-1})
3−6	1.51 (fixed)	1.4 (fixed)	0.9 (fixed)	$1.95^{+0.06}_{-0.06}$	$2.30^{+0.04}_{-0.04}$
6−30	1.51 (fixed)	1.4 (fixed)	4.2 (fixed)	$2.45^{+0.07}_{-0.07}$	$3.89^{+0.11}_{-0.15}$
3−6	1.50 (fixed)	1.44 (fixed)	0.9 (fixed)	$1.91^{+0.06}_{-0.06}$	$2.30^{+0.09}_{-0.11}$
6−30	1.50 (fixed)	1.44 (fixed)	4.2 (fixed)	$2.33^{+0.06}_{-0.06}$	$3.83^{+0.09}_{-0.11}$
3−6	1.49 (fixed)	1.48 (fixed)	0.9 (fixed)	$1.90^{+0.05}_{-0.05}$	$2.39^{+0.10}_{-0.14}$
6−30	1.49 (fixed)	1.48 (fixed)	4.2 (fixed)	$2.24^{+0.06}_{-0.06}$	$3.89^{+0.10}_{-0.13}$

Note.
[a] Unabsorbed PWN flux in the corresponding energy bands.

Table 5
PWN Model Input Parameters

Parameter	Value
SNR Parameters	
Explosion Energy E_{sn}	8.9×10^{50} erg
Ejecta Mass M_{ej}	$20.9\ M_\odot$
ISM Density n_{ism}	8.5×10^{-3} cm^{-3}
Distance D	6.2 kpc
PWN Parameters	
Wind Magnetization η_B	2.4×10^{-3}
Minimum e$^{\pm}$ Injection Energy E_{min}	10 GeV
Maximum e$^{\pm}$ Injection Energy E_{max}	400 TeV
Particle Index p_1	2.29
Particle Index p_2	2.42
External Photon Field Temperature T_{ic}	2750 K
External Photon Field Normalization $K_{ic} a T_{ic}^4$	25.3 eV cm^{-3}
Pulsar Parameters	
Spin-down Timescale τ_{sd}	3.57 kyr
Braking Index p	1.90

the pulsar and PWN and indicates that the PWN contributes substantially up to ∼30 keV.

Since we found that the joint XMM-Newton–NuSTAR spectra contains significant curvature, we also fit the spectrum in the 3−6 and 6−30 keV bands individually. We did this while allowing the N_H values to vary, and we fixed the N_H values to the corresponding values in Table 3. These results are shown in Table 4 and are the observational data points that we use in our SED modeling in Section 4.

A power-law distribution $\frac{dN}{dE}$ of synchrotron cooling $e^{\pm}$ with an initial constant particle spectral index p will develop a particle spectrum break $\Delta p = 1$, corresponding to an observed photon spectral break $\Delta\Gamma = 0.5$ (N. S. Kardashev 1962; G. B. Rybicki & A. P. Lightman 1979; S. P. Reynolds 2009). The $\Delta\Gamma \approx 0.5$ spectral break at $E_{break} \approx 5$ keV is therefore consistent with the synchrotron cooling. A synchrotron cooling break will be observed in a system of synchrotron-emitting particles at a photon energy E_{break} if the corresponding particle energy E at the synchrotron spectrum peak,

$$E_{break} = h\nu_{peak} = 0.29 \times \frac{3}{2}\left(\frac{E}{m_e c^2}\right)^2\left(\frac{eB}{m_e c}\right), \quad (1)$$

is equal to the system age τ. If we know τ, then the value of E_{break} can then be used to estimate the system's magnetic field strength:

$$E_{break} = 168\left(\frac{B}{5\ \mu\ \mathrm{G}}\right)^{-2}\left(\frac{\tau}{3\ \mathrm{kyr}}\right)^{-1}\ \mathrm{TeV}. \quad (2)$$

The SED modeling presented in Section 4 makes an independent estimate of the PWN age τ and magnetic field B and therefore provides an independent estimate of E_{break}.

4. SED Modeling

With the benefit of hard X-ray constraints from NuSTAR, we can extend the G54.1+0.3 SED dynamical modeling described in J. D. Gelfand et al. (2015). Given phyical input parameters (Table 5), this one-zone, energy-conserving radiative model that tracks the time evolution of the G54.1+0.3 system

Table 6
Observed Properties of the G54.1+0.3 System alongside the Model-predicted Properties

Property	Observed	Model	References
Pulsar Properties			
$\dot{E}$	1.2×10^{37} erg s^{-1}	Fixed	(1)
$\tau_{\rm char}$	2900 yr	Fixed	(1)
PWN Properties			
PWN Radius $\theta_{\rm pwn}$	1.′14 ± 0.′04	1.′13	(2, 3)
0.15 GHz Flux Density	464 ± 47 mJy	459	(4)
1.4 GHz Flux Density	433 ± 30 mJy	432	(2)
4.7 GHz Flux Density	327 ± 25 mJy	331	(2)
8.5 GHz Flux Density	252 ± 20 mJy	261	(2)
Flux (3−6 keV)[a]	$2.30_{-0.11}$–$2.39^{+0.11}$	2.16	This work
Photon Index Γ(3−6 keV)	$1.90_{-0.05}$–$1.95^{+0.06}$	2.04	This work
Flux (6−30 keV)[a]	$3.83_{-0.11}$–$3.89^{+0.11}$	3.90	This work
Photon Index Γ(6−30 keV)	$2.24_{-0.06}$–$2.45^{+0.07}$	2.56	This work
535 MeV Photon Density[b]	$<3.14 \times 10^{-6}$	1.10×10^{-6}	(5)
1.7 GeV Photon Density[b]	$(2.23 \pm 0.80) \times 10^{-7}$	1.62×10^{-7}	(5)
5.4 GeV Photon Density[b]	$(1.33 \pm 0.56) \times 10^{-8}$	2.09×10^{-8}	(5)
17.3 GeV Photon Density[b]	$(2.03 \pm 0.67) \times 10^{-9}$	2.49×10^{-9}	(5)
55.1 GeV Photon Density[b]	$<5.10 \times 10^{-10}$	2.68×10^{-10}	(5)
176 GeV Photon Density[b]	$(2.67 \pm 2.09) \times 10^{-11}$	2.53×10^{-11}	(5)
311 GeV Photon Density[b]	$(1.10 \pm 0.56) \times 10^{-11}$	7.92×10^{-12}	(6)
492 GeV Photon Density[b]	$(4.2 \pm 1.4) \times 10^{-12}$	3.06×10^{-12}	(6)
780 GeV Photon Density[b]	$(1.12 \pm 0.45) \times 10^{-12}$	1.02×10^{-12}	(6)
1.2 TeV Photon Density[b]	$(6.2 \pm 1.7) \times 10^{-13}$	3.90×10^{-13}	(6)
3.0 TeV Photon Density[b]	$(3.1 \pm 2.1) \times 10^{-14}$	5.2×10^{-14}	(6)
25−100 TeV Photon Index Γ	3.11 ± 0.12	2.69	(7)
25−100 TeV Differential Flux[c] N_0	0.64 ± 0.06	0.66	(7)
χ^2 (dof)	...	28.9 (8)	

Notes.
[a] Unabsorbed flux in units of 10^{-12} erg s^{-1} cm^{-2}.
[b] Photon density in units of photons s^{-1} cm^{-2} TeV^{-1}.
[c] $\frac{dN}{dE} = N_0\left(\frac{E}{50\,\rm TeV}\right)^{-\Gamma}$ with N_0 in units of 10^{-16} photons s^{-1} cm^{-2} TeV^{-1}.
References. (1) F. Camilo et al. (2002); (2) C. C. Lang et al. (2010); (3) F. J. Lu et al. (2002); (4) G. H. Heald et al. (2015); (5) J. L. Eagle (2022); (6) V. A. Acciari et al. (2010); (7) Z. Cao et al. (2024).

(J. D. Gelfand et al. 2009). The model predicts the broadband PWN SED and the sizes on the SNR and PWN, and it is constrained by the presently measured values of the pulsar period P and period derivative $\dot{P}$ (S. Hattori et al. 2020; M. Abdelmaguid et al. 2023; S. M. Straal et al. 2023; I. Pope et al. 2024).

Table 6 lists the observed properties of the G54.1+0.3 system along with the values predicted by the best-fit model. The uncertainty in the pulsar X-ray flux and photon index contributes a systematic uncertainty to the G54.1+0.3 PWN X-ray spectrum. For the purposes of this modeling, we adopt the range X-ray fluxes and photon indices listed in Table 4, corresponding to a range in values of the pulsar spectrum photon index (1.40−1.48). Following the methodology of S. Hattori et al. (2020), we consider all values of the X-ray fluxes within this range are equally consistent with the model, and we accordingly only add values outside of this range when calculating the χ^2 values.

In addition to the original data points described in J. D. Gelfand et al. (2015), we also include a 150 MHz radio data radio flux and several γ-ray photon densities in this new analysis. This low-frequency 150 MHz radio data point was obtained from the LOFAR data archive (G. H. Heald et al. 2015). The new Fermi γ-ray data points were obtained from J. L. Eagle (2022). We also include some of the LHAASO γ-ray data reported by Z. Cao et al. (2024). The 1−25 TeV LHAASO flux is significantly higher than the VERITAS data (V. A. Acciari et al. 2010), likely due to the contribution of one or more unrelated sources, and we plot this flux in gray in Figure 5 for reference but do not fit to it in our PWN modeling. We do include the 25−100 TeV LHAASO flux in our modeling. The 25−100 TeV LHAASO flux is reported as the best fit to an assumed power law, while our PWN model predicts a more detailed spectral curvature in this band.

Table 5 lists the best-fit model input parameters, all of which were varied to fit the PWN SED and angular size. The $\chi^2 = 28.9$ (8 degrees of freedom, dof) statistic is dominated by the deviation of the photon index Γ from the LHAASO photon index. This is expected because the PWN model predicts spectral curvature in this band, while at this time only a power-law fit has yet been reported by LHAASO. The observed 25−100 TeV LHAASO flux is in excellent agreement with the model-predicted value. In Figure 5 we have plotted the SED predicted by the best-fit PWN dynamical evolution model.

5. Discussion

5.1. Comparison with Previous Work

J. D. Gelfand et al. (2015) modeled G54.1+0.3's SED, without the additional hard X-ray, low-frequency radio and γ-ray

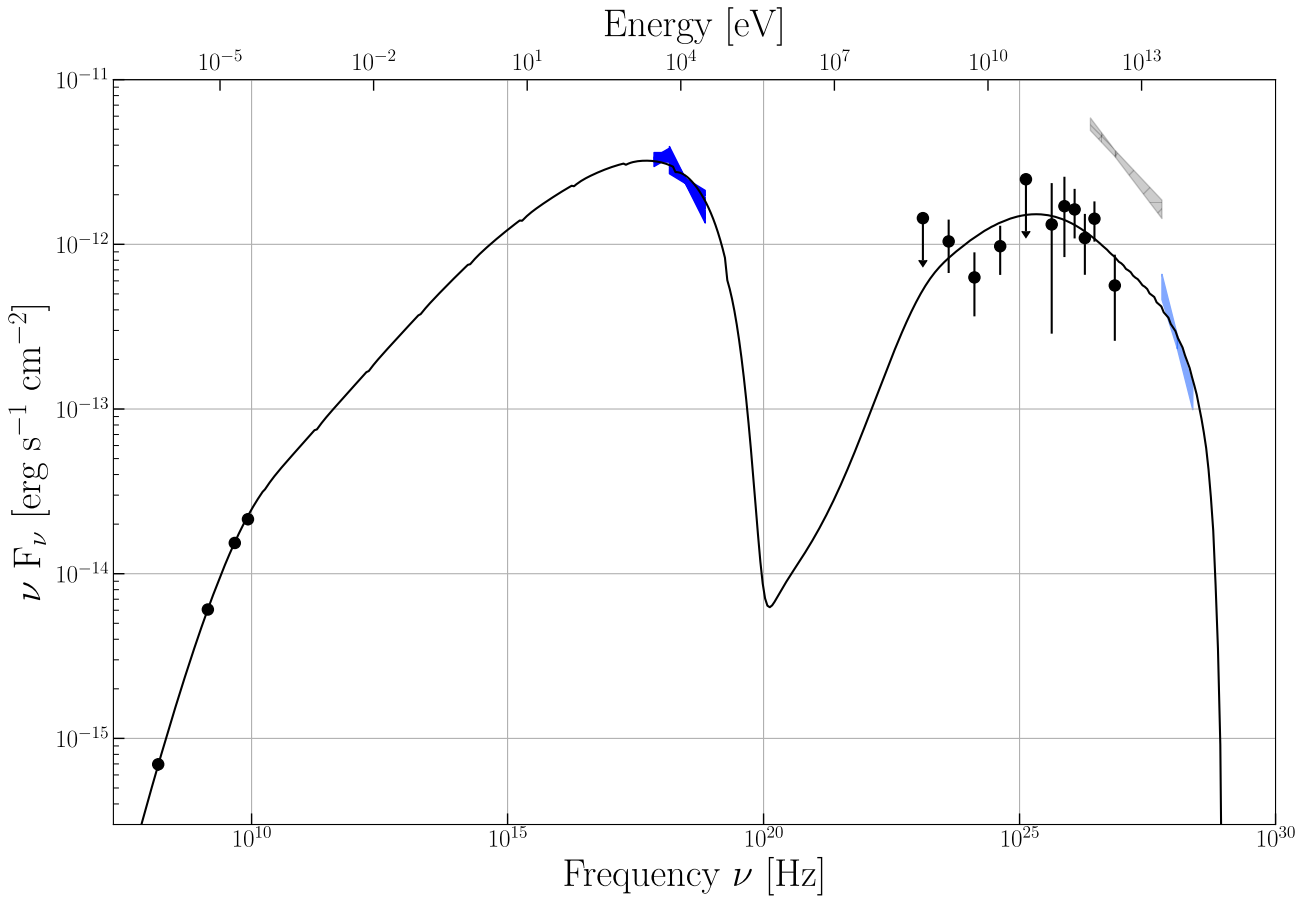

Figure 5. A PWN dynamical evolution model fit to the broadband SED (and radius) of the PWN in G54.1+0.3. The model is described in Section 4, the input model parameters are given in Table 5, and the model predictions are compared to the observed properties of the G54.1+0.3 system in Table 6.

data considered in this analysis. Also, J. D. Gelfand et al. (2015) fit the PWN model to a SNR size, which we have not done in this analysis, since the SNR detection is now uncertain.

The NuSTAR data analysis presented in this paper has allowed us to constrain the maximum particle energy in the PWN. The best-fit model predicts a maximum particle energy of ≈0.4 PeV, which is significantly less than the best-fit value 0.96−2700 PeV range that J. D. Gelfand et al. (2015) calculated without the constraints from this NuSTAR data.

The best-fit values of the explosion energy, ejecta mass, and interstellar medium (ISM) density are comparable to those found by J. D. Gelfand et al. (2015), though J. D. Gelfand et al. (2015) found that there are degeneracies between some model parameters, and a full exploration of the model parameter space is left for future work. We also find a small value of wind magnetization parameter $\eta_B \sim 10^{-3}$, comparable to other PWNe. Interestingly, we found that G54.1's particle spectrum is roughly consistent with a single particle index, with the two particle indices p_1 and p_2 differing by only 0.13. Most PWNe require two particle spectral indices differing by ∼0.5 to simultaneously account for their X-ray and radio spectra. This suggests that there may be a diversity of particle acceleration mechanisms operating in PWNe.

We find that a ≈2750 K photon field is required for our model to reproduce the γ-ray data points. G54.1+0.3 is embedded within a cluster of OB stars, with spectra much hotter than ≈2750 K. A photon field resembling a blackbody with a ≈2750 K temperature may be produced after the light from these hot OB stars is reprocessed by the dust known to surround G54.1+0.3.

This PWN model predicts a magnetic field $B \approx 7\ \mu$G and a PWN age of 2830 yr, which corresponds to a break energy of ≈8 keV (see Equations (1) and (2)). This is remarkably close to the value of the break observed at ≈5 keV. If the spectral break observed at 5 keV is due to synchrotron cooling, then this suggests that our SED modeling has correctly predicted the PWN magnetic field strength and age.

5.2. Comparison with Other Young PWNe

Table 7 lists some of the properties of the G54.1+0.3 system, derived in this paper and in previous studies, with the properties of other young ($\lesssim$5 kyr) PWNe. Table 7 lists these PWNe in order of decreasing spin-down power and demonstrates that G54.1+0.3 is not particularly powerful for its age. PSR J1930 +1852 has a relatively long spin-down timescale τ_{sd}, comparable to G21.5-0.9 and much longer than Kes 75 and HESS J1640 −465. The PWN in G54.1+0.3 also has the low PWN magnetization parameter η_B, while PSR J1930+1852's dipole magnetic field is comparable to the other systems. PSR J1930+1852's spin-down luminosity is also typical among these other young PWNe.

Using the spin-down timescale and braking index in Table 5, we have calculated the pulsar's initial spin period P_0 by setting the time t equal to the pulsar true age $\tau_{true} \approx 2800$ yr,

$$P_0 = P\left(1 + \frac{t}{\tau_{sd}}\right)^{\frac{1}{1-n}} = 72\ \text{ms}, \quad (3)$$

Table 7
Young Pulsars Powering PWNe

Pulsar	SNR	P (ms)	$\dot{P}$ (10^{-14} s s^{-1})	$\dot{E}$ (10^{36} erg s^{-1})	$\tau_{\rm char.}$ (kyr)	B (10^{12} G)	P_0 (ms)	η_B	$E_{\rm max}$ (PeV)	References
PSR B0531+21	Crab	33	42.1	450	1.2	3.8	≈20	...	...	(1)
PSR B0540−69	SNR 0540−69.3	51	47.9	150	1.7	4.9	≈40	...	...	(1)
PSR J1833−1034	G21.5−0.9	62	20.2	33	4.8	3.2	≈20	3.2×10^{-3}	0.3	(2)
PSR J0205+6449	3C 58	66	19.3	27	5.4	2.9	≈50	...	...	(1)
PSR B1509−58	MSH 15−52	152	153	18	1.6	15	≈10	...	...	(1)
PSR J1124−5916	G292.0+1.8	135	76.4	12	2.9	4.3	≈40	...	...	(1)
PSR J1930+1852	**G54.1+0.3**	**137**	**75.1**	**12**	**2.9**	**4.3**	**≈72**	**2.4×10^{-3}**	**0.4**	**This work**
PSR J1846−0258	Kes 75	327	710	8.1	0.73	50	≈200	0.12	1.1	(3)
PSR J1640−4631	G338.3−0.0	206	97.6	4.4	3.4	14	≈10	0.07	1.24	(4)

Note. P and $\dot{P}$ values are taken from the ATNF pulsar catalog. $\tau_{\rm char} \equiv \frac{P}{2\dot{P}}$ $B \equiv 3.2 \times 10^{19}\sqrt{P\dot{P}}$ P_0 is the initial pulsar spin period. η_B is the fraction of neutron star's spin-down luminosity injected as magnetic energy.
References: (1) (R. A. Chevalier 2005); (2) (S. Hattori et al. 2020); (3) (E. V. Gotthelf et al. 2021; S. M. Straal et al. 2023); (4) (E. V. Gotthelf et al. 2014; M. Abdelmaguid et al. 2023).

and the initial spin period derivative $\dot{P}_0$,

$$\dot{P}_0 = \frac{P_0}{\tau_{\rm sd}(p-1)} = 7.1 \times 10^{-13}\,{\rm s\,s^{-1}}. \quad (4)$$

These parameters correspond to an initial spin-down power $\dot{E}_0 = 7.5 \times 10^{37}\,{\rm erg\,s^{-1}}$ and initial spin-down-measured dipole field $B_0 = 7.2 \times 10^{12}\,{\rm G}$. We see that the spin-down power of Kes 75 and G54.1+0.3 has decreased from their initial values much less than the decrease inferred for HESS J1640−465 and G21.5-0.9. A future measurement of PSR J1930+1852's braking index would allow for a more detailed comparison of G54.1+0.3 with other young PWNe.

Previous NuSTAR studies of young PWNe such as Crab and 3C 58 found that the PWN size shrinks with increasing energy (K. K. Madsen et al. 2015; H. An 2019). This "synchrotron burn-off" effect probes particle transport within these PWNe and may also be important to understand the structure of G54.1+0.3. It is unclear if there is a significant "synchrotron burn-off" in the case of PWN G54.1+0.3; the NuSTAR PSF is unfortunately comparable to the apparent size of the PWN (demonstrating the need for hard X-ray observatories with higher spatial resolution; S. Reynolds et al. 2023).

6. Summary

We have analyzed spectral and timing data from previously unpublished NuSTAR observations of PWN G54.1+0.3 powered by PSR J1930+1852. PWN G54.1+0.3 is clearly detected up to ≈70 keV, with spectral curvature in the 3−30 keV band. Modeling the PWN SED with the benefit of this NuSTAR data, and also new radio and γ ray data, suggests that the maximum particle energy $E_{\rm max} \sim 400$ TeV. A future pulsar timing analysis and exploration of the PWN model parameter space can better constrain parameters such as the braking index n, the spin-down timescale $\tau_{\rm sd}$, and the initial pulsar spin period P_0.

Acknowledgment

J.G. acknowledges NuSTAR grant F8732 and NYUAD research grant AD022. Center for Astrophysics and Space Science (CASS) acknowledges support from NYUAD Institute, which is funded by the government of Abu Dhabi through the administration of Tamkeen. G.Z. acknowledges support from the China Manned Space Program with grant No. CMS-CSST-2025-A13.

ORCID iDs

J. A. J. Alford https://orcid.org/0000-0002-2312-8539
G.-B. Zhang https://orcid.org/0000-0001-8630-5435
J. D. Gelfand https://orcid.org/0000-0003-4679-1058

References

Abdelmaguid, M., Gelfand, J. D., Gotthelf, E., et al. 2023, ApJ, 946, 40
Acciari, V. A., Aliu, E., Arlen, T., et al. 2010, ApJL, 719, L69
An, H. 2019, ApJ, 876, 150
Arnaud, K. A. 1996, in ASP Conf. Ser. 101, Astronomical Data Analysis Software and Systems V, 101, ed. G. H. Jacoby & J. Barnes (San Francisco, CA: ASP), 17
Bocchino, F., Bandiera, R., & Gelfand, J. 2010, A&A, 520, A71
Camilo, F., Lorimer, D. R., Bhat, N. D. R., et al. 2002, ApJL, 574, L71
Cao, Z., Aharonian, F., An, Q., et al. 2024, ApJS, 271, 25
Chevalier, R. A. 2005, ApJ, 619, 839
Eagle, J. L. 2022, PhD thesis, Clemson
Gelfand, J. D., Slane, P. O., & Temim, T. 2015, ApJ, 807, 30
Gelfand, J. D., Slane, P. O., & Zhang, W. 2009, ApJ, 703, 2051
Goedhart, S., Cotton, W. D., Camilo, F., et al. 2024, MNRAS, 531, 649
Gotthelf, E. V., Safi-Harb, S., Straal, S. M., et al. 2021, ApJ, 908, 212
Gotthelf, E. V., Tomsick, J. A., Halpern, J. P., et al. 2014, ApJ, 788, 155
Harrison, F. A., Craig, W. W., Christensen, F. E., et al. 2013, ApJ, 770, 103
Hattori, S., Straal, S. M., Zhang, E., et al. 2020, ApJ, 904, 32
Heald, G. H., Pizzo, R. F., Orrú, E., et al. 2015, A&A, 582, A123
Kardashev, N. S. 1962, SvA, 6, 317
Lang, C. C., Wang, Q. D., Lu, F., & Clubb, K. I. 2010, ApJ, 709, 1125
Leahy, D. A., Darbro, W., Elsner, R. F., et al. 1983, ApJ, 266, 160
Lu, F., Wang, Q. D., Gotthelf, E. V., et al. 2007, ApJ, 663, 315
Lu, F. J., Wang, Q. D., Aschenbach, B., Durouchoux, P., & Song, L. M. 2002, ApJL, 568, L49
Madsen, K. K., Reynolds, S., Harrison, F., et al. 2015, ApJ, 801, 66
Pope, I., Mori, K., Abdelmaguid, M., et al. 2024, ApJ, 960, 75
Reynolds, S., An, H., Abdelmaguid, M., et al. 2023, FrASS, 10, 1321278
Reynolds, S. P. 2009, ApJ, 703, 662
Rybicki, G. B., & Lightman, A. P. 1979, A Wiley-interscience Publication (New York: Wiley), 1979
Slane, P. 2017, Handbook of Supernovae (Berlin: Springer), 2159
Straal, S. M., Gelfand, J. D., & Eagle, J. L. 2023, ApJ, 942, 103
Temim, T., Dwek, E., Arendt, R. G., et al. 2017, ApJ, 836, 129
Temim, T., Slane, P., Reynolds, S. P., et al. 2010, ApJ, 710, 309
Tsalapatas, K., Arias, M., Shimwell, T., et al. 2024, A&A, 690, A247
Wilms, J., Allen, A., & McCray, R. 2000, ApJ, 542, 914